Correction of concomitant gradient artifacts in experimental microtesla MRI

Whittier R. Myers *, Michael Mößle, John Clarke

Department of Physics, University of California, Berkeley, CA 94720-7300, USA
Materials Sciences Division, Lawrence Berkeley National Laboratory, Berkeley, CA 94720, USA

Abstract

Magnetic resonance imaging (MRI) suffers from artifacts caused by concomitant gradients when the product of the magnetic field gradient and the dimension of the sample becomes comparable to the static magnetic field. To investigate and correct for these artifacts at very low magnetic fields, we have acquired MR images of a 165-mm phantom in a 66-μT field using gradients up to 350 μT/m. We prepolarize the protons in a field of about 100 mT, apply a spin-echo pulse sequence, and detect the precessing spins using a superconducting gradiometer coupled to a superconducting quantum interference device (SQUID). Distortion and blurring are readily apparent at the edges of the images; by comparing the experimental images to computer simulations, we show that concomitant gradients cause these artifacts. We develop a non-perturbative, post-acquisition phase correction algorithm that eliminates the effects of concomitant gradients in both the simulated and the experimental images. This algorithm assumes that the switching time of the phase-encoding gradient is long compared to the spin precession period. In a second technique, we demonstrate that raising the precession field during phase encoding can also eliminate blurring caused by concomitant phase-encoding gradients; this technique enables one to correct concomitant gradient artifacts even when the detector has a restricted bandwidth that sets an upper limit on the precession frequency. In particular, the combination of phase correction and precession field cycling should allow one to add MRI capabilities to existing 300-channel SQUID systems used to detect neuronal currents in the brain because frequency encoding could be performed within the 1–2 kHz bandwidth of the readout system.

1. Introduction

Although the current trend is to increase the magnetic field employed in magnetic resonance imaging (MRI), in the past 10 years there has been renewed interest in MRI at fields below 100 mT. Low-field MRI is primarily used for prepolarized proton imaging [1–6] and for hyperpolarized noble gas imaging [7–11]. Such experiments detect spin precession using either conventional Faraday coils [1–3,7,9–11] or superconducting input circuits coupled to superconducting quantum interference devices (SQUIDs) [4–6,8,12]. The precession field (B_0) employed in these experiments ranges from 7.8 μT to 25 mT. The potential benefits of low-field MRI include reduced system costs, more open coil geometries [13], reduced susceptibility artifacts [7], and increased proton T_1 contrast [14]; T_1 is the longitudinal relaxation time. In addition to the technical challenge of achieving a signal-to-noise ratio (SNR) sufficient to produce high-quality images, low-field MRI faces the fundamental problem of image distortion and blurring caused by concomitant magnetic field gradients.

Magnetic resonance imaging requires magnetic field gradients to map the spatial position of a given spin onto its precession frequency or phase. An ideal imaging gradient would establish a linear relationship between position and precession frequency over the entire sample volume.

* Corresponding author. Fax: +1 510 642 1304.
E-mail address: wmyers@berkeley.edu (W.R. Myers).

However, Maxwell's equations prohibit unidirectional magnetic field gradients. Any physical gradient contains unwanted fields orthogonal to and of the same magnitude as the desired imaging gradient. Such concomitant gradients cause the precession frequency to be a nonlinear function of position, distorting the resulting MR image. Norris and Hutchison [15] first brought the issue of concomitant gradients to the attention of the MRI community in 1990. More recently, Yablonskiy et al. [16] quantified the impact of concomitant gradients by demonstrating that concomitant gradients warp planes of constant precession frequency into cylinders of radius $R_c = B_0/G$, where G is the strength of the applied gradient; concomitant gradient distortion becomes significant when R_c becomes comparable to the field of view L. The parameter $\varepsilon = L/R_c$ characterizes the severity of concomitant gradient distortion. For typical high-field MRI, $B_0 \sim 1$ T and $G \sim 10$ mT/m, so that $R_c \sim 100$ m, and the effects of concomitant gradients can be neglected for human-sized objects using conventional sequences. In contrast, McDermott et al. [4] perform SQUID-detected MRI with $B_0 = 132$ μT and $G = 200$ μT/m, yielding $R_c = 0.7$ m. While the resulting image distortion cannot be seen in their images of 35-mm phantoms, concomitant gradient distortion would almost certainly be observable in an image of a human brain, roughly 0.2 m across, using the same imaging parameters.

A number of different schemes have been proposed to mitigate the effects of concomitant gradients in MRI. Radical schemes include alternating the direction of the precession field [17], applying higher order gradients along with the imaging gradient [18], and employing a train of 180° pulses and stroboscopic acquisition [19]. These methods require substantial modifications of MRI hardware and pulse sequences and have not been demonstrated in practice. Other methods focus on fast imaging sequences at 1.5 T and above. Weisskoff et al. [20] apply "prewarping" frequency-encoding gradients before the 180° pulse in echo-planar imaging to reduce the average amplitude of the concomitant phase. Bernstein, Zhou, and co-workers [21–23] demonstrate phase correction algorithms that reduce concomitant gradient distortion in spiral and echo-planar images. These algorithms correct only the first-order perturbation of precession frequency by concomitant gradients and have not been shown to work at low fields. Volegov et al. [24] compute the higher-order effects of concomitant gradients on the point spread function in low-field MRI when the gradient switching time is much shorter than the precession period, but do not provide details of a correction algorithm.

In this paper, we consider the effects of concomitant gradients on MR images of human-scale objects in microtesla magnetic fields in the limit of slow gradient switching. One motivation for our work is the possibility of combining low-field MRI with existing systems for magnetic source imaging (MSI) of the brain. Such systems contain about 300 SQUIDs in a helmet placed over the head of the subject and are used to detect the magnetic fields produced by neu-

ronal currents in the brain. Needless to say, our techniques could be applied to other applications of low-field MRI.

We begin by simulating the acquisition of a MR image of a 0.175-m two-dimensional grid of spins using a pulse sequence with $B_0 = 66$ μT, a 57 μT/m frequency-encoding gradient, and a 280 μT/m maximum phase-encoding gradient. The concomitant terms of the frequency-encoding gradient distort the image, while the concomitant terms of the phase-encoding gradient cause image blurring. We next develop a non-perturbative phase correction algorithm that can also correct for inhomogeneous magnetic fields. We demonstrate this correction algorithm on both the simulated images and experimental images generated using comparable sequence parameters. We introduce a new technique showing that raising B_0 during phase encoding can mitigate image blurring caused by concomitant phase-encoding gradients. Finally, we conclude by considering the limits of these correction techniques and the constraints that concomitant gradients place on low-field MRI hardware and the design of pulse sequences.

2. Theory and algorithms

For simplicity, this paper considers only the case of two-dimensional MRI with B_0 pointing in the z-direction and the sample in the yz-plane. Frequency encoding is performed along the y-direction, phase encoding along the z-direction. The results can be generalized to alternate geometries and to three dimensions.

2.1. Effect of concomitant gradients on MR images

Fig. 1 shows an encoding sequence for standard spin-echo MRI with echo time 2τ and data acquisition time T_{acq}. The phase-encoding gradient is ramped up for a time
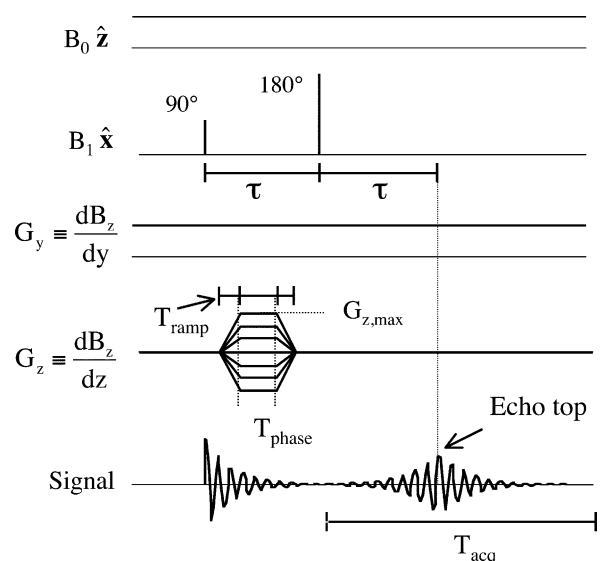

Fig. 1. Spin-echo pulse sequence employed in the simulations and experiments described in this paper. Data acquisition begins after the 180° pulse, and the echo top occurs a time τ after the 180° pulse.

T_{ramp}, held constant for T_{phase}, and then ramped down for T_{ramp}. If we ignore the requirements of Maxwell's equations, the ideal phase-encoding magnetic field is

$$\mathbf{B}_{phase}^{ideal} = (B_0 + yG_y + zG_z)\hat{\mathbf{z}}, \tag{1}$$

where G_y and G_z are the magnitude of the frequency and phase-encoding gradients, respectively. Similarly, the ideal magnetic field during data acquisition (frequency encoding) is

$$\mathbf{B}_{freq}^{ideal} = (B_0 + yG_y)\hat{\mathbf{z}}. \tag{2}$$

For these fields, the spin precession angular frequency ($\gamma|\mathbf{B}|$, where γ is the gyromagnetic ratio) is a linear function of position. Therefore, the image can be reconstructed as the Fourier transform of k-space. However, Maxwell's equations require $\nabla \cdot \mathbf{B} = 0$ and $\nabla \times \mathbf{B} = 0$ for static magnetic fields in free space. Thus, the physical magnetic fields used in MRI must contain additional concomitant gradient terms. Assuming no field inhomogeneity and using a cylindrically symmetrical coil to generate G_z, we can express the physical fields as (Eq. (A10) with $\alpha = 1/2$ in [25]):

$$\mathbf{B}_{phase}^{phys} = \mathbf{B}_{phase}^{ideal} + zG_y\hat{\mathbf{y}} - \frac{1}{2}xG_z\hat{\mathbf{x}} - \frac{1}{2}yG_z\hat{\mathbf{y}}, \tag{3}$$

$$\mathbf{B}_{freq}^{phys} = \mathbf{B}_{freq}^{ideal} + zG_y\hat{\mathbf{y}}. \tag{4}$$

To illustrate the effect of these concomitant gradient terms, the spin-precession angular frequency during phase and frequency encoding can be expanded in the yz-plane to second order as [25]

$$
\begin{aligned}
\omega_{phase}^{phys} &= \gamma\left|\mathbf{B}_{phase}^{phys}\right| \\
&= \gamma\left[B_0 + G_y y + G_z z + \frac{G_y^2}{2B_0}z^2 + \frac{G_z^2}{8B_0}y^2 - \frac{G_y G_z}{2B_0}yz + O\left(\frac{G^3}{B_0^2}\right)\right]
\end{aligned}
\tag{5}
$$

and

$$\omega_{freq}^{phys} = \gamma\left|\mathbf{B}_{freq}^{phys}\right| = \gamma\left[B_0 + G_y y + \frac{G_y^2}{2B_0}z^2 + O\left(\frac{G_y^3}{B_0^2}\right)\right]. \tag{6}$$

The additional concomitant gradient terms cause the precession frequency to be a nonlinear function of position. Linearity is restored in the limit in which the magnetic field $GL/2$ generated by the gradient coils at the edge of the sample is much smaller than B_0 ($\varepsilon/2 \equiv GL/2B_0 \ll 1$) [16].

Because the mathematical properties of Eqs. (3) and (4) have been adequately explored elsewhere [16,25], this paper focuses on the effects of concomitant gradients on MR images. Fig. 2A shows a simulated MR image of a 175 mm × 175 mm grid of spins using the pulse sequence of Fig. 1 and the idealized magnetic fields of Eqs. (1) and (2). The grid is the approximate size of a human brain. We choose $B_0 = 66\ \mu T$, $G_y = 57\ \mu T/m$ and the area under the phase-encoding gradient to match the experimental sequences presented in Section 3. A detailed description of the simulation algorithm is reserved for Appendix A. Fig. 2B shows a simulated image using the same sequence
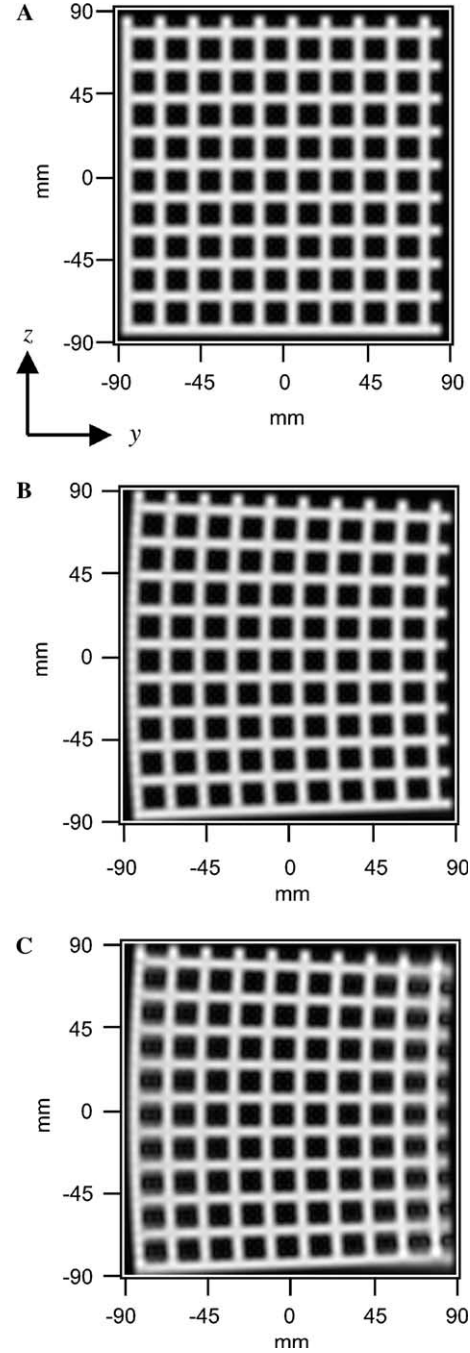

Fig. 2. MRI simulations of the effect of concomitant gradients using the pulse sequence of Fig. 1. (A) $B_0 = 66\ \mu T$, $G_y = 57\ \mu T/m$, 79 phase encoding steps, $\tau = T_{phase} = 100\ ms$, and $G_{z,max} = 39\ \mu T/m$; concomitant gradients omitted. (B) Same parameters as A, concomitant gradients included. (C) Same as (B) except $T_{phase} = 14\ ms$ and $G_{z,max} = 280\ \mu T/m$. All simulations assume that the gradient ramp time T_{ramp} is long enough so that the magnetization adiabatically follows the direction of the applied field ($\gamma B_0 T_{ramp} \gg 1$ [16]), but short enough to neglect the phase accumulated during gradient ramping.

and the physical magnetic fields from Eqs. (3) and (4). Concomitant gradients distort Fig. 2B by bending the vertical edges of the image towards $+y$, by stretching the vertical scale for $y < 0$, and by compressing the vertical scale for $y > 0$. Fig. 2C shows a simulated image that employs a

phase-encoding gradient seven times higher than Fig. 2B and correspondingly shorter T_{phase}; short phase-encoding times are desirable because they prevent signal loss caused by spin relaxation during phase encoding. In addition to the distortion present in Fig. 2B, Fig. 2C shows vertical blurring at the horizontal edges of the image.

The image distortion and blurring in Figs. 2B and C can be explained using Eqs. (5) and (6). The apparent position of a spin in the frequency-encoding direction to second order is given by

$$y_{\text{MRI}} = \frac{\omega_{\text{freq}}^{\text{phys}} - \gamma B_0}{\gamma G_y} \approx y + \frac{G_y}{2B_0} z^2. \tag{7}$$

Thus, spins with large $|z|$ appear shifted towards $+y$, as seen in Fig. 2B. The apparent position of a spin in the z-direction depends on its phase at the echo top

$$\begin{aligned} \phi_{\text{echo}}^{\text{phys}} &= -\omega_{\text{phase}}^{\text{phys}} T_{\text{phase}} - \omega_{\text{freq}}^{\text{phys}}\left(\tau - T_{\text{phase}}\right) + \omega_{\text{freq}}^{\text{phys}}\tau \\ &= -\left(\omega_{\text{phase}}^{\text{phys}} - \omega_{\text{freq}}^{\text{phys}}\right)T_{\text{phase}}, \end{aligned} \tag{8}$$

according to the relation

$$z_{\text{MRI}} = \frac{-\phi_{\text{echo}}^{\text{phys}}}{\gamma G_z T_{\text{phase}}} \approx \left(1 - \frac{G_y}{2B_0}y\right)z + \frac{G_z}{8B_0}y^2; \tag{9}$$

terms higher than second order have again been neglected and $T_{\text{ramp}} = 0$. The term in parenthesis describes the vertical scale distortion seen in Fig. 2B. Because each phase-encoding step employs a different value of G_z, z_{MRI} takes on different values in the same image, and images employing high G_z (such as Fig. 2C) will be blurred at large $|y|$.

2.2. Reconstruction algorithm to correct distortion and blurring

Although the distortion caused by frequency-encoding concomitant gradients shown in Fig. 2B could be corrected by undoing the spatial shifts described in Eqs. (7) and (9) (or their higher-order counterparts) after image reconstruction, the blurring caused by phase-encoding concomitant gradients demonstrated in Fig. 2C cannot be corrected after reconstruction. Here we present a post-acquisition, pre-reconstruction phase correction algorithm to correct for image distortion and blurring caused by concomitant gradients. Our algorithm applies the concepts developed by Du et al. [23] in the context of high-field echo-planar imaging to low-field spin-echo imaging and extends their algorithm beyond second-order correction. We show that it can be further extended to correct for systematic image distortions caused by magnetic field inhomogeneity.

We begin by separating the spin precession angular frequency during the frequency-encoding step into two parts

$$\omega_{\text{freq}}^{\text{phys}} = \gamma\left|\mathbf{B}_{\text{freq}}^{\text{ideal}}\right| + \Delta\omega_{\text{freq}}^{\text{c}} = \omega_{\text{freq}}^{\text{ideal}} + \Delta\omega_{\text{freq}}^{\text{c}}, \tag{10}$$

where $\Delta\omega_{\text{freq}}^{\text{c}}$ is the change in angular precession frequency caused by concomitant gradients. We next generalize Eq. (8) to allow for the possibility of non-negligible T_{ramp}:

$$\phi_{\text{echo}}^{\text{phys}} = -\gamma\int_0^\tau \left|\mathbf{B}_{\text{phase}}^{\text{phys}}(t)\right|dt + \omega_{\text{freq}}^{\text{phys}}\tau, \tag{11}$$

where $\mathbf{B}_{\text{phase}}^{\text{phys}}(t)$ is the magnetic field including concomitant gradients at a time t after the 90° pulse. Although $\mathbf{B}_{\text{phase}}^{\text{phys}}(t)$ changes direction while the gradient is ramped, the precessing spins remain perpendicular to $\mathbf{B}_{\text{phase}}^{\text{phys}}(t)$ in the adiabatic gradient switching regime $\gamma B_0 T_{\text{ramp}} \gg 1$ [16]. In this regime, the precession frequency depends on the magnitude of $\mathbf{B}_{\text{phase}}^{\text{phys}}(t)$ rather than its components and the spin phase remains well defined during gradient ramping. We separate $\phi_{\text{echo}}^{\text{phys}}$ into two parts

$$\begin{aligned} \phi_{\text{echo}}^{\text{phys}} &= \left(-\gamma\int_0^\tau \left|\mathbf{B}_{\text{phase}}^{\text{ideal}}(t)\right|dt + \omega_{\text{freq}}^{\text{ideal}}\tau\right) \\ &\quad + \Delta\phi_{\text{echo}}^{\text{c}} = \phi_{\text{echo}}^{\text{ideal}} + \Delta\phi_{\text{echo}}^{\text{c}}. \end{aligned} \tag{12}$$

Here $\mathbf{B}_{\text{phase}}^{\text{ideal}}(t)$ is defined analogously to $\mathbf{B}_{\text{phase}}^{\text{phys}}(t)$, and $\Delta\phi_{\text{echo}}^{\text{c}}$ is the change in the spin phase at the echo top caused by concomitant gradients.

The magnetic field measured at the detector for a given phase-encoding gradient G_z can be computed by integrating the contribution of each spin over the volume of the sample

$$\begin{aligned} B_{\text{det}}(t; G_z) &\propto \int\int_V\int M(\mathbf{r}) \\ &\quad \times \cos\left(\omega_{\text{freq}}^{\text{ideal}}t + \phi_{\text{echo}}^{\text{ideal}} + \Delta\omega_{\text{freq}}^{\text{c}}t + \Delta\phi_{\text{echo}}^{\text{c}}\right)d\mathbf{r}. \end{aligned} \tag{13}$$

Here $M(\mathbf{r})$ is the magnetization at point $\mathbf{r}$, and t is defined relative to the echo top. The four terms inside the parenthesis are implicit functions of $\mathbf{r}$; $\phi_{\text{echo}}^{\text{ideal}}$ and $\Delta\phi_{\text{echo}}^{\text{c}}$ depend on the phase-encoding gradient G_z as well. We can formally eliminate the contributions of concomitant gradients near a specific point $\mathbf{r}_0$ by defining a scaled time

$$t' = \left(\frac{\omega_{\text{freq}}^{\text{ideal}}}{\omega_{\text{freq}}^{\text{ideal}} + \Delta\omega_{\text{freq}}^{\text{c}}}\right)\left(t - \frac{\Delta\phi_{\text{echo}}^{\text{c}}}{\omega_{\text{freq}}^{\text{ideal}}}\right). \tag{14}$$

Here, $\omega_{\text{freq}}^{\text{ideal}}$, $\Delta\omega_{\text{freq}}^{\text{c}}$, $\phi_{\text{echo}}^{\text{ideal}}$, and $\Delta\phi_{\text{echo}}^{\text{c}}$ are evaluated at $\mathbf{r}=\mathbf{r}_0$ so that t' depends on $\mathbf{r}_0$ and G_z. We then evaluate Eq. (13) by inserting t' in place of t to obtain a rescaled detected field

$$\begin{aligned} B_{\text{det}}'(t; G_z) &= B_{\text{det}}(t'; G_z) \\ &\propto \int\int_V\int M(\mathbf{r})\cos\left(\omega_{\text{freq}}^{\text{ideal}}t + \phi_{\text{echo}}^{\text{ideal}}\right)d\mathbf{r}, \end{aligned} \tag{15}$$

which eliminates the terms $\Delta\omega_{\text{freq}}^{\text{c}}$ and $\Delta\phi_{\text{echo}}^{\text{c}}$. If we record $B_{\text{det}}(t; G_z)$ for each value of G_z, we can turn this formal manipulation into a prescription for correcting concomitant gradients by first breaking the image up into regions, each centered on a particular value of $\mathbf{r}_0$. For each value of $\mathbf{r}_0$, we interpolate the acquired data to obtain $B_{\text{det}}'(t; G_z)$, evaluating Eq. (14) at the position $\mathbf{r}_0$. Subsequently we demodulate and combine $B_{\text{det}}'(t; G_z)$ to obtain a k-space representation of the image. The inverse Fourier

transform of this k-space will be corrected for concomitant gradients in the vicinity of $\mathbf{r}_0$. Finally, we splice together the images obtained for each value of $\mathbf{r}_0$; the resulting image will be globally corrected for concomitant gradient distortion and blurring.

An equivalent algorithm can be performed directly on the k-space representation of the distorted image. Demodulation of $B_{\text{det}}(t; G_z)$ can be represented as

$$S(k_y, k_z) = \text{Lowpass}\left\{ B_{\text{det}}\left(\frac{k_y}{\gamma G_y}; G_z\right) \exp\left(-\mathrm{i}\frac{B_0 k_y}{G_y}\right) \right\},$$
(16)

where S represents the complex k-space, $k_y = \gamma G_y t$, $k_z = -\gamma \int_0^\tau G_z \, dt$, and Lowpass represents the action of a low-pass filter. We define $k_y' = \gamma G_y t'$ to find

$$
\begin{aligned}
S'(k_y, k_z) &= S\left(k_y', k_z\right) \\
&= \text{Lowpass}\left\{ B_{\text{det}}\left(\frac{k_y'}{\gamma G_y}; G_z\right) \exp\left(-\mathrm{i}\frac{B_0 k_y'}{G_y}\right) \right\}.
\end{aligned}
$$
(17)

The inverse Fourier transform of $S'(k_y, k_z)$ will be corrected for concomitant gradients in the vicinity of $\mathbf{r}_0$; a globally corrected image can be created by splicing locally corrected images together.

To demonstrate this phase correction algorithm, we applied it to the k-space data generated by the MRI simulation used to produce the distorted and blurred image in Fig. 2C. To reconstruct the image, we divided the field of view into equally spaced square regions. We evaluated Eq. (17) to compute $S'(k_y, k_z)$ for each region, choosing $\mathbf{r}_0$ at the center of that region. Fig. 3A shows the results of this algorithm using 8×8 square regions. The blurring is eliminated, and the grid lines are globally straight; the only remaining artifacts are discontinuities at the boundaries of the correction regions. We can eliminate these discontinuities by reducing the size of the correction regions as shown in Fig. 3B, which employs 24×24 square regions. Alternately, we can apply the post-reconstruction local image-warping algorithm described in Appendix B; Fig. 3C shows the results of this algorithm applied to Fig. 3A. Fig. 3C has a few remaining artifacts, but the image-warping algorithm is substantially faster than increasing the grid density because it requires fewer reconstruction regions to eliminate discontinuities, thereby reducing the number of interpolation and Fourier transform steps. It takes about 30 s to reconstruct Fig. 3C using unoptimized code running on a 1.6 GHz PowerPC G5. Since each region can be reconstructed independently of the others, this algorithm could be easily adapted for parallel processing. Table 1 summarizes the fields and gradients of the corrected images.

To estimate the accuracy of the phase correction algorithm, we consider a spin located at a point $\mathbf{r}_0 + \Delta\mathbf{r} = (y_0 + \Delta y, z_0 + \Delta z)$ in the vicinity of $\mathbf{r}_0$. The combined effect of concomitant gradients and phase correction shifts the detected frequency to
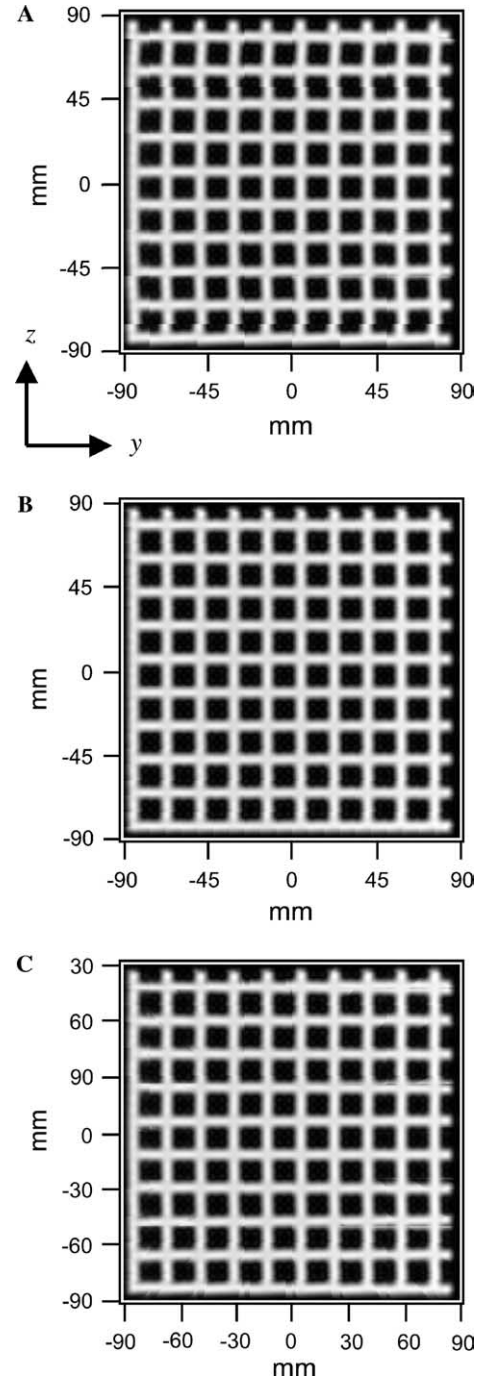

Fig. 3. Concomitant gradient correction algorithm applied to the k-space used to generate Fig. 2C. (A) 8×8 correction regions. (B) 24×24 correction regions. (C) 8×8 correction regions using local image warping.

$$
\begin{aligned}
\omega_{\text{freq}}^{\text{corr}} &= \left(\frac{\omega_{\text{freq}}^{\text{phys}}(\mathbf{r}_0 + \Delta\mathbf{r})}{\omega_{\text{freq}}^{\text{phys}}(\mathbf{r}_0)} \right) \omega_{\text{freq}}^{\text{ideal}}(\mathbf{r}_0) \\
&= \gamma B_0 \frac{\sqrt{\left(1 + \chi_y + \Delta\chi_y\right)^2 + \left(\chi_z + \Delta\chi_z\right)^2}}{\sqrt{\left(1 + \chi_y\right)^2 + \chi_z^2}} \left(1 + \chi_y\right),
\end{aligned}
$$
(18)

where $\chi_y = G_y y_0 / B_0$, $\chi_z = G_y z_0 / B_0$, $\Delta\chi_y = G_y \Delta y / B_0$, and $\Delta\chi_z = G_y \Delta z / B_0$. Factoring the denominator out of the numerator yields

Table 1
Sequence parameters and correction algorithms

Image	Figures	Encoding step	B_0 (µT)	G_y or $G_{z,max}$ (µT/m)	$\varepsilon = GL/B_0$[a]	Required concomitant gradient correction
Simulated grid image	2B, 2C, 3	Frequency	66	57	0.15	Phase correction
	2B	Phase	66	39	0.10	
	2C, 3	Phase	66	280	0.74	
Experimental grid image	6	Frequency	66	57	0.14	Phase correction
	6	Phase	66	280[b]	0.70	
Simulated limits of concomitant gradient correction	8B, 8C	Frequency	35	98	0.49	Phase correction and B_0 field cycling
	8B, 8C	Phase	100	590	1.03	

[a] For the simulated images, $L = 175$ mm; for the experimental images, $L = 165$ mm.
[b] Root mean square gradient. Maximum phase-encoding gradient is 350 µT/m.

$$\omega_{freq}^{corr} = \gamma B_0$$
$$\times \sqrt{1 + \frac{\Delta\chi_y(2 + 2\chi_y + \Delta\chi_y) + \Delta\chi_z(2\chi_z + \Delta\chi_z)}{(1 + \chi_y)^2 + \chi_z^2}(1 + \chi_y)}. \quad (19)$$

In Section 4, we show that the concomitant gradient correction algorithm requires $G_y L/B_0 < 1$, so that χ_y and χ_z must always be less than $1/2$. If we employ a 10×10 or larger grid of correction regions, $\Delta\chi_y$, and $\Delta\chi_z$ will be much smaller than χ_y and χ_z. Assuming χ_y, χ_z, $\Delta\chi_y$, and $\Delta\chi_z$ are all much smaller than unity, we can expand Eq. (19) to first order in $\Delta\chi$ and second order in χ as

$$\omega_{freq}^{corr} = \gamma B_0 \left(1 + \chi_y + \Delta\chi_y + \chi_z\Delta\chi_z - \chi_y\chi_z\Delta\chi_z - \chi_z^2\Delta\chi_y + O(\chi^3)\right). \quad (20)$$

The apparent position of the spin can be computed by substituting ω_{freq}^{corr} for ω_{freq}^{phys} in Eq. (7)

$$y_{MRI}^{corr} \approx y_0 + \Delta y + \frac{G_y}{B_0}z_0\Delta z - \frac{G_y^2}{B_0^2}y_0 z_0\Delta z - \frac{G_y^2}{B_0^2}z_0^2\Delta y. \quad (21)$$

The first two terms in Eq. (21) are the physical location of the spin, and the latter terms represent the remaining concomitant gradient distortion. Comparing the third term in Eq. (21) to the second term in Eq. (7), we see that the leading error term now scales as $z_0\Delta z$ instead of z^2; concomitant gradient correction will therefore be effective when $\Delta z \ll z_0$. This third term in Eq. (21) describes the discontinuities in the vertical lines in Fig. 3A at large values of $|z|$. These discontinuities can be corrected either by reducing Δy and Δz by reducing the size of the correction regions (Fig. 3B) or by employing the local image-warping algorithm that corrects for terms linear in Δy and Δz (Fig. 3C). There is a similar but more complicated analysis for the phase-encoding direction.

This phase correction algorithm can be extended to correct distortions arising from known field inhomogeneities in addition to concomitant gradients by simply adding the appropriate field terms to Eqs. (3) and (4). Inhomogeneities in B_0, the background field, and the frequency-encoding gradient G_y should be added to both Eqs. (3) and (4), while inhomogeneity in the phase-encoding gradient G_z should be added to Eq. (3) only. We apply software correction for background field inhomogeneity to experimental images in Section 3.

2.3. Precession field cycling to eliminate phase-encoding concomitant gradient blurring

Concomitant gradients can also be mitigated in low-field MRI by employing pulse sequences that cannot be implemented with high-field superconducting magnets. These pulse sequences can supplement or replace the software correction algorithm described above and must be tailored to fit specific applications. For example, consider the proposals [4,26] to combine MSI of the brain with MRI by detecting MR signals with the array of SQUIDs used to measure magnetic fields in MSI equipment. Because neuronal currents in the brain change on a timescale of 1 ms or slower, the bandwidth of existing MSI systems is typically 1–2 kHz, thereby limiting the potential MRI readout frequency. In the MRI sequence shown in Fig. 1, we must choose $T_{phase} \ll T_2$ (the transverse spin relaxation time) to minimize signal losses caused by relaxation; for brain tissue, T_2 ranges from 60 to 100 ms [27]. Choosing $T_{phase} = 10$ ms and resolution $\Delta z = 2$ mm requires a maximum phase-encoding gradient $G_{z,max} = \pi/\gamma T_{phase} \Delta z = 590$ µT/m. Since this gradient corresponds to a field of 59 µT at the edges of the 0.2 m field of view required for head imaging, we require $B_0 > 59$ µT (2.5 kHz) simply to maintain the one-to-one relation between spatial position and precession frequency; the results of Section 4 suggest that B_0 must be at least twice this field for successful software correction of concomitant gradient distortion. Protons precessing at the frequencies associated with these fields would not be detected by existing MSI systems.

The solution to this problem makes use of the fact that substantially lower gradients are required to achieve a given resolution in the frequency-encoding direction than in the phase-encoding direction. The resolution in the frequency-encoding direction depends on the acquisition time after the echo top, $(T_{acq} - \tau)$; we require $(T_{acq} - \tau) \sim T_2$ and $\tau \ll T_2$ to maximize the SNR. Choosing $(T_{acq} - \tau) = 60$ ms requires a frequency-encoding gradient $G_y = \pi/\gamma(T_{acq} - \tau)\Delta y = 98$ µT/m to achieve a resolution

$\Delta y = 2$ mm. We can therefore employ the pulse sequence shown in Fig. 4, in which we increase the precession field to $B_{0,\text{phase}}$ to reduce the effects of concomitant gradients during phase encoding, and then lower it during data acquisition to allow detection of the precessing spins in a limited bandwidth.

Fig. 5 shows a simulated MR image generated with the pulse sequence of Fig. 4 applied to the grid of Fig. 2. The sequence parameters are the same as Fig. 2C except that B_0 has been increased by a factor of four during the phase-encoding step. The blurring at the edges of Fig. 2C caused by concomitant gradients during phase encoding has vanished; Fig. 5 is essentially identical to Fig. 2B, in which the maximum phase-encoding gradient is seven times smaller. The remaining distortion can be corrected using
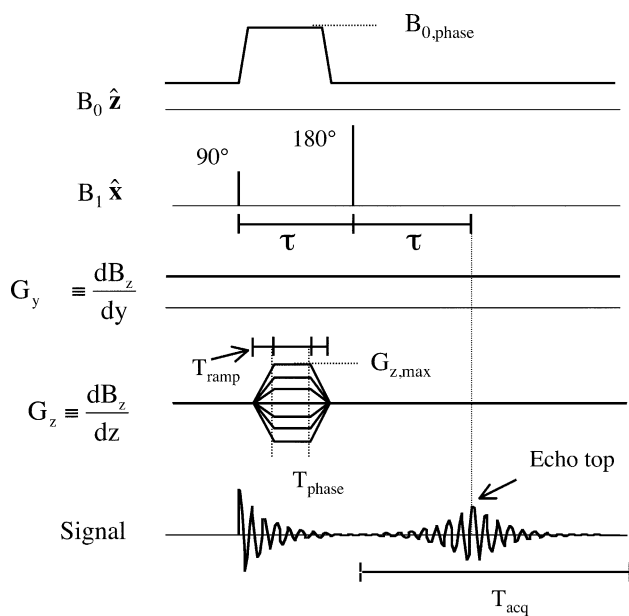

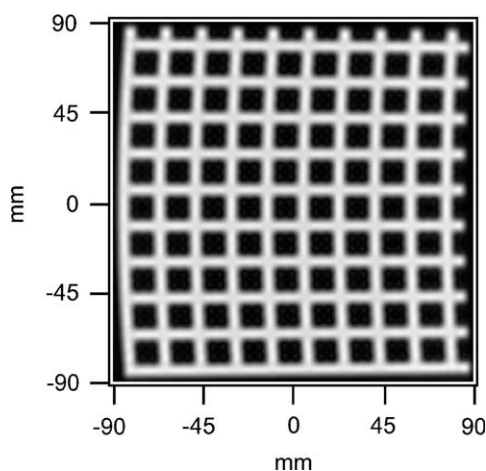Fig. 4. Field-cycling pulse sequence for MRI at readout frequencies below 2 kHz.

Fig. 5. MRI simulation of the pulse sequence of Fig. 4 with $B_{0,\text{phase}} = 264$ µT; all other parameters as in Fig. 2C.

either the methods of Section 2.2 or post-reconstruction image-warping algorithms.

3. Experimental results

We employed our microtesla MRI system to obtain all experimental images presented in this paper. This system consists of copper-wire coils wound on wooden or G-10 fiberglass supports that provide the necessary polarizing, precession, excitation, and gradient fields; [4,28] describe this system in detail. We prepolarized the protons in a field of about 100 mT and then turned off this field adiabatically so that the spins aligned along the B_0 field. We next applied the pulse sequence shown in Fig. 1. A superconducting wire-wound gradiometer coupled to a SQUID detected the magnetic field from the precessing spins. We demodulated the resulting data in software to obtain a k-space representation of the image and then reconstructed the image with an inverse fast Fourier transform.

To observe the distortion and blurring caused by concomitant gradients in experimental images, we created a physical analogue of the pattern of spins shown in Fig. 2A by machining 20 5-mm wide, 165-mm long, 14-mm deep grooves in a sheet of plastic and filling them with water. We placed this grid on top of the polarizing coil and suspended the liquid helium dewar containing the gradiometer and SQUID above the grid. Because the 65-mm gradiometer pickup loop restricted the available field of view, we could not acquire the entire image with one pulse sequence. We therefore acquired a series of nine images, moving the gradiometer after each image to span the entire grid. The center of the gradiometer occupied positions $y = 0, \pm 60$ mm and $z = 0, \pm 60$ mm relative to the center of the grid. We employed techniques used in multiple-coil MRI reconstruction [29] to merge the nine images into a single composite image and compensate for the inhomogeneous sensitivity of the gradiometer.

We applied the pulse sequence of Fig. 1 with $B_0 = 66$ µT and $G_y = 57$ µT/m to image the grid. Because the experimental gradients have nonzero rise times, whereas the MRI simulation algorithm assumes $T_{\text{ramp}} = 0$, the experimental phase-encoding gradient waveform differed from that used to generate Fig. 2C. Since the area under the phase-encoding gradient waveform determines the resolution of the image and the time-integrated square of the gradient determines the first-order concomitant gradient effects, we matched these quantities in the simulated and experimental pulse sequences. Fig. 6A shows the resulting image. Concomitant gradients cause distortion and blurring comparable to that seen in Fig. 2C, but Fig. 6A contains asymmetric distortion not present in Fig. 2C. This distortion originates from inhomogeneity in the Earth's magnetic field that we believe is caused by steel reinforcing rods in the floor of our laboratory. Rather than construct additional gradient shimming coils to cancel this inhomogeneous field, we measured its influence on the spin precession frequency at the center, edges, and corners of the grid. The precession frequency differed by 25 Hz at opposite cor-
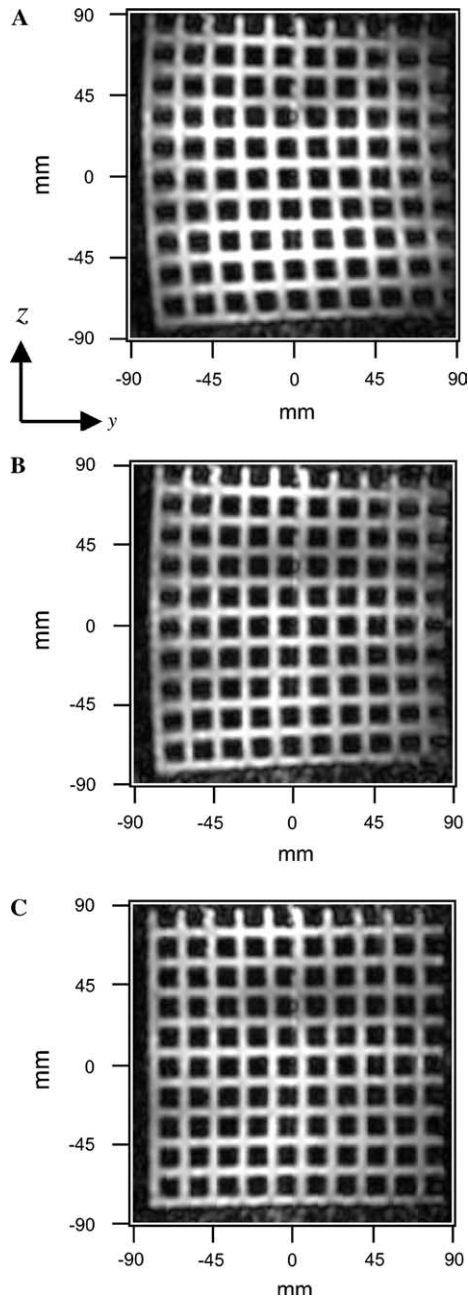
Fig. 6. Experimental MR images using the pulse sequence of Fig. 1 with $B_0 = 66 \, \mu T$, $G_y = 57 \, \mu T/m$, $G_{z,max} = 350 \, \mu T/m$, 79 phase encoding steps, $T_{phase} = 5 \, ms$, $T_{ramp} = 5 \, ms$, and $\tau = 100 \, ms$. (A) Uncorrected. (B) Corrected for measured background field inhomogeneity. (C) Corrected for concomitant gradients and background field inhomogeneity. Both corrected images use 16×16 correction regions with local image warping.
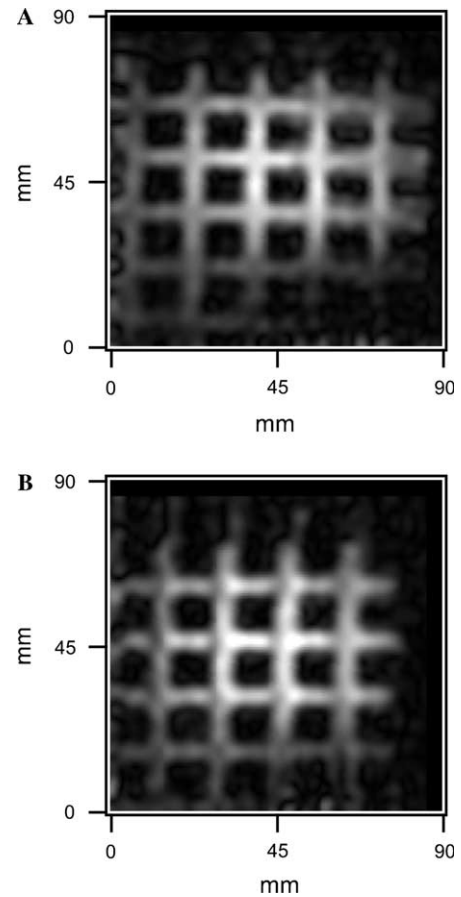

Fig. 7. Experimental MR images demonstrating correction for phase encoding concomitant gradient blurring using field cycling. Top right corner of the grid imaged with (A) the pulse sequence of Fig. 1 with parameters given in Fig. 6. (B) the field-cycling pulse sequence of Fig. 4 with $B_{0,phase} = 264 \, \mu T$ and all other parameters as in Fig. 6. We applied the phase correction algorithm to both images to correct for the inhomogeneity in the earth's field but not for concomitant gradients.

ners of the grid. We fitted a two-dimensional quadratic function to this data and used the phase correction algorithm to correct the distortion caused by the inhomogeneous field. The resulting image, shown in Fig. 6B, has distortion and blurring nearly identical to Fig. 2C. We then applied both the empirical field correction and the concomitant gradient correction to obtain the image shown in Fig. 6C. The combination of these corrections eliminates the blurring and produces an image that is nearly distortion-free.

We also investigated the effect of raising the precession field during phase encoding on concomitant gradient blurring. Fig. 7A shows an enlarged view of the top-left corner of Fig. 6A, and Fig. 7B shows the same corner imaged with the same pulse sequence except that we raised B_0 to 264 μT during phase encoding. The blurring caused by concomitant phase-encoding gradients in Fig. 7A is not present in Fig. 7B, consistent with the simulation shown in Fig. 5. We attempted to expand the field of view by combining field-cycling images from different gradiometer positions, but were not able to do so because none of our available amplifiers could both cycle B_0 up to 264 μT for phase encoding and maintain a stable measurement field of 66 μT for the duration of the experiment without coupling excess field noise into the gradiometer.

4. Limits of concomitant gradient correction

So far, we have only considered cases in which the phase correction algorithm or B_0 field cycling successfully eliminates distortion and blurring caused by concomitant gradi-

ents. However, these correction techniques must fail for arbitrarily low B_0. If we reduce B_0 sufficiently, the field generated by the gradient coils will become comparable to B_0 and the total magnetic field will have a minimum within the image field of view. Spins on either side of this minimum cannot be distinguished by their precession frequencies, and neither correction technique accounts for this situation. This criterion restricts the allowable fields and gradients during both frequency and phase encoding.

During frequency encoding, the z-component of the magnetic field is weakest and the perpendicular y-component strongest at the points $(y, z) = (-L/2, \pm L/2)$, where L is the image field of view. The magnitude of the magnetic field at this point is

$$
\left| \mathbf{B}_{\text{freq}}^{\text{phys}} \right| = \sqrt{\left(B_0 - \frac{1}{2}LG_y \right)^2 + \left(\frac{1}{2}LG_y \right)^2}
$$
$$
= B_0 \sqrt{\left(1 - \frac{1}{2}\varepsilon_y^{\text{freq}} \right)^2 + \left(\frac{1}{2}\varepsilon_y^{\text{freq}} \right)^2}, \tag{22}
$$

where $\varepsilon_y^{\text{freq}} = G_y L / B_0$. Since Eq. (22) has a minimum at $\varepsilon_y^{\text{freq}} = 1$, we require $\varepsilon_y^{\text{freq}} < 1$ to keep the minimum of the magnetic field outside the field of view. During phase encoding when $G_z = G_{z,\text{max}}$, the z-component of the magnetic field is weakest at the point $(-L/2, -L/2)$. At this point

$$
\left| \mathbf{B}_{\text{phase}}^{\text{phys}} \right| = \sqrt{\left(B_{0,\text{phase}} - \frac{1}{2}LG_y - \frac{1}{2}LG_{z,\text{max}} \right)^2 + \left(-\frac{1}{2}LG_y + \frac{1}{4}LG_{z,\text{max}} \right)^2}
$$
$$
= B_{0,\text{phase}}
$$
$$
\times \sqrt{\left(1 - \frac{1}{2}\varepsilon_y^{\text{phase}} - \frac{1}{2}\varepsilon_z^{\text{phase}} \right)^2 + \left(-\frac{1}{2}\varepsilon_y^{\text{phase}} + \frac{1}{4}\varepsilon_z^{\text{phase}} \right)^2}, \tag{23}
$$

where $\varepsilon_y^{\text{phase}} = G_y L / B_{0,\text{phase}}$ and $\varepsilon_z^{\text{phase}} = G_{z,\text{max}} L / B_{0,\text{phase}}$. To keep the minima of Eq. (23) outside the field of view we require $\partial |\mathbf{B}_{\text{phase}}^{\text{phys}}| / \partial \varepsilon_y^{\text{phase}} < 0$ and $\partial |\mathbf{B}_{\text{phase}}^{\text{phys}}| / \partial \varepsilon_z^{\text{phase}} < 0$, which translate into the conditions $\varepsilon_y^{\text{phase}} + \varepsilon_z^{\text{phase}} / 4 < 1$ and $\varepsilon_y^{\text{phase}} / 4 + 5\varepsilon_z^{\text{phase}} / 8 < 1$. While these expressions describe analytical limits beyond which concomitant gradient correction will fail, more stringent conditions may be required to produce acceptable image quality.

To investigate the limits of concomitant gradient correction further, we simulate the effect of progressively lowering B_0 in the 2-mm resolution pulse sequence for combined MRI/MSI described in Section 2.3. Fig. 8A shows the grid image reconstructed from this pulse sequence with $B_0 = B_{0,\text{phase}} = 35 \, \mu\text{T}$ (1490 Hz), $G_y = 98 \, \mu\text{T/m}$ and $G_{z,\text{max}} = 590 \, \mu\text{T/m}$; because B_0 is lower and the gradients are higher than in the experimental pulse sequence, concomitant gradient distortion and blurring are greater than in Fig. 2C or Fig. 6B. In this sequence, the 80 ms acquisition time is substantially longer than $\tau = 20$ ms, where 2τ is the echo time, and we therefore employ an iterative algorithm to reconstruct the image from the resulting partial k-space [30]. Fig. 8B shows the results of the same
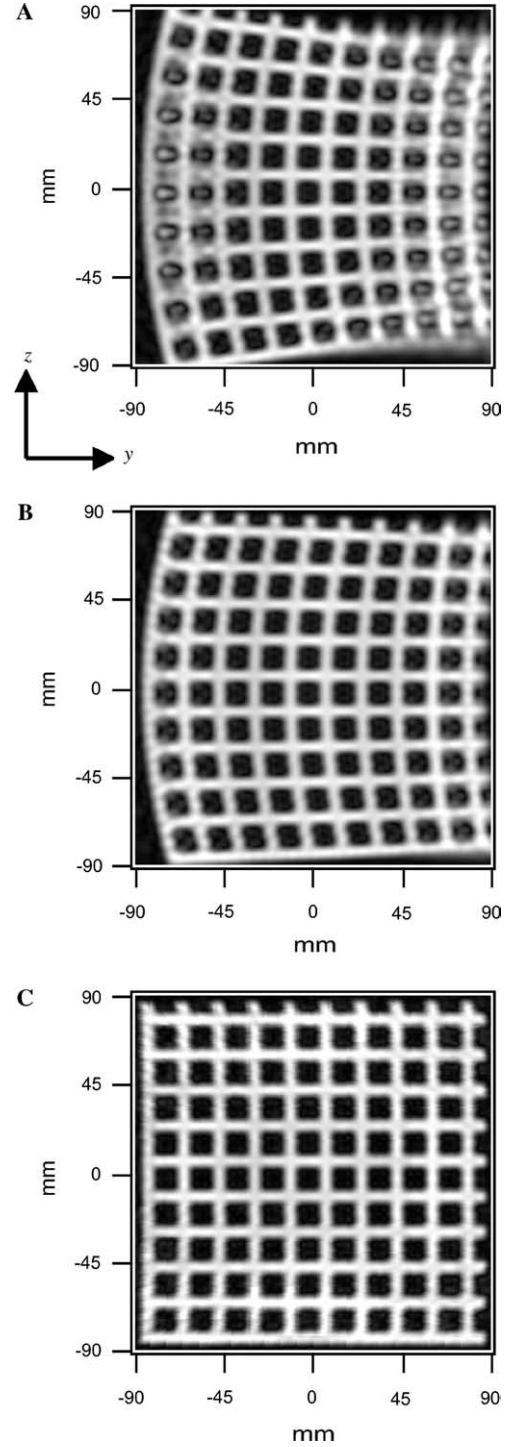

Fig. 8. MRI simulations of an ultra-low-field pulse sequence for 2-mm resolution brain imaging. (A) $B_0 = B_{0,\text{phase}} = 35 \, \mu\text{T}$, $G_y = 98 \, \mu\text{T/m}$, 101 phase encoding steps, $G_{z,\text{max}} = 590 \, \mu\text{T/m}$, $T_{\text{phase}} = 10$ ms, $\tau = 20$ ms, and $T_{\text{acq}} = 80$ ms. (B) Same as (A) except $B_{0,\text{phase}} = 100 \, \mu\text{T}$. (C) Concomitant gradient correction algorithm using 24×24 reconstruction regions and local image warping applied to the k-space used to generate (B).

sequence except with $B_{0,\text{phase}} = 100 \, \mu\text{T}$. In this case, raising B_0 during phase encoding only partially corrects the blurring caused by concomitant phase-encoding gradients. Applying the phase correction algorithm to the k-space

used to generate Fig. 8B yields Fig. 8C; 24 × 24 reconstruction regions and local image warping are required to generate an artifact-free image. We repeated this procedure with $B_0 = 23.5$ µT (1000 Hz), but the resulting image is unacceptably distorted and blurred despite field cycling to 100 µT and applying the phase correction algorithm. We therefore conclude that a precession field of at least 35 µT during data acquisition is required to achieve 2-mm resolution of head-sized objects using this sequence; the electronics of a combined MRI/MSI system would have to be capable of detecting the 1490 ± 420 Hz signal band of the precessing spins (assuming $L = 0.2$ m). Because the external noise in our laboratory increases rapidly below 2.5 kHz and the effectiveness of the aluminum eddy-current shield surrounding our system decreases at low frequencies, we were unable to perform experimental MRI below 2.8 kHz to test these results.

In addition to the limitations on B_0 and gradient strength discussed above, the phase correction algorithm requires $\gamma B_0 T_{\text{ramp}} \gg 1$ to ensure that the spins remain perpendicular to the direction of the total magnetic field during gradient ramping. For $B_0 = 35$ µT, we require $T_{\text{ramp}} \gg 0.1$ ms, a small fraction of the 10 ms phase-encoding time used for Fig. 8.

5. Discussion

We have developed a non-perturbative phase correction algorithm to eliminate concomitant gradient artifacts in low-field MRI in the limit of adiabatic gradient switching. We have also shown that increasing B_0 during phase encoding can reduce blurring caused by concomitant phase-encoding gradients. We have demonstrated these techniques on the largest SQUID-detected microtesla MR images yet taken. Although we obtained the experimental images in this paper by translating a single SQUID gradiometer to nine different positions, this technique mimics the performance of an array of nine gradiometers operating in parallel.

Table 1 summarizes the fields and gradients of the experimental (Fig. 6) and simulated (Figs. 2, 3, and 8) images presented in this paper. The phase correction algorithm alone is enough to correct the concomitant gradient distortion and blurring seen in Figs. 2C and 6B. In contrast, the lower B_0 and higher gradients employed in Fig. 8 require both increasing B_0 during phase encoding and post-acquisition correction. These techniques enable distortion-free MRI in regimes in which ε becomes comparable to unity, thereby extending the potential of low-field MRI. In particular, they should enable the acquisition of MR images of the brain within the limited bandwidth of existing MSI systems.

Acknowledgments

Appendix A. MRI simulation algorithm

We created the simulated MR images employed in this paper by calculating the signal detected by SQUID gradiometer as a function of time from a given object and pulse sequence and then processing these simulated traces with our image reconstruction software. We assume that the distance between the object and the bottom loop of the gradiometer is much smaller than the gradiometer baseline, so that the gradiometer effectively operates as a magnetometer. We employed the following algorithm to generate the time traces:

1. Divide the simulated object into squares of constant spin density. We employ $\Delta y = \Delta z = 6$ mm squares for the grid images presented in this paper; 3-mm squares produce nearly identical images.
2. Calculate the magnetic field at the center of the square during frequency and phase-encoding steps and the resulting values of $\omega_{\text{freq}}^{\text{phys}}$ and $\phi_{\text{echo}}^{\text{phys}}$ using Eqs. (3), (4), and (8) for each value of G_z.
3. Calculate the contribution of the nth square to the field detected by the SQUID as

$$B_n(t) \propto \rho_n \int_{-\Delta y/2}^{\Delta y/2} \int_{-\Delta z/2}^{\Delta z/2} \cos \left[\left(\omega_{\text{freq}}^{\text{phys}} + \gamma y' G_y \right) \left(t - T_{\text{phase}} \right) \right. \\ \left. + \phi_{\text{echo}}^{\text{phys}} - \gamma z' G_z T_{\text{phase}} \right] \text{d}z' \, \text{d}y', \qquad (24)$$

where ρ_n is the spin density of the nth square and the 180° pulse occurs at $t = 0$. This equation assumes the slow gradient ramping regime ($\gamma B_0 T_{\text{ramp}} \gg 1$) in which the precessing spins remain perpendicular to the total magnetic field at all times and the accumulated phase scales with the time integral of the total field. It also ignores spin relaxation and assumes uniform detector response over the sample. We solve this integral analytically, then evaluate with numerical values.
4. Sum $B_n(t)$ for all squares to obtain $B(t)$ for this value of G_z.

Appendix B. Local image warping algorithm

The phase correction algorithm ensures that the image intensity at the correction point $\mathbf{r}_0$ corresponds to the true spin density at that point. However, Fourier transform image reconstruction assumes uniform frequency and phase-encoding gradients over the entire image. Concomitant gradients modify the local gradient values, causing image distortion and discontinuities at the boundaries of the cor-

rection regions as seen in Fig. 3A. We can eliminate these artifacts by increasing the number of correction regions, as in Fig. 3B, but the time to run the phase correction algorithm scales with the number of regions required. Alternatively, we can reduce or eliminate these discontinuities without substantially increasing the run time by applying a linear transformation to each corrected region based on the calculated gradients at $\mathbf{r}_0 = (y_0, z_0)$. By examining Eqs. (7) and (9), we can express the apparent position in the locally corrected image (y_{MRI}, z_{MRI}) in terms of the true spin position (y, z) to first order as

$$y_{MRI} - y_0 = \frac{1}{\gamma G_y} \left[\frac{\partial \omega_{freq}^{phys}}{\partial y} (y - y_0) + \frac{\partial \omega_{freq}^{phys}}{\partial z} (z - z_0) \right] \quad (25)$$

and

$$z_{MRI} - z_0 = \frac{-1}{\gamma G_z T_{phase}} \left[\frac{\partial \phi_{echo}^{phys}}{\partial y} (y - y_0) + \frac{\partial \phi_{echo}^{phys}}{\partial z} (z - z_0) \right]. \quad (26)$$

We obtain the inverse linear transformation by solving these equations to obtain $y(y_{MRI}, z_{MRI})$ and $z(y_{MRI}, z_{MRI})$; applying this transform to each locally corrected image corrects for first-order gradient variation. The partial derivatives of ω_{freq}^{phys} and ϕ_{echo}^{phys} can be evaluated either analytically or numerically. Eq. (26) should be evaluated using a small value of G_z since local image warping cannot correct distortion from concomitant phase-encoding gradients. Fig. 3C shows the results of this algorithm applied using 8×8 square correction regions; all subsequent applications of the phase correction algorithm in this paper employ local image warping.

References

[1] G. Planinsic, J. Stepisink, M. Kos, Relaxation-time measurement and imaging in the earth's magnetic field, J. Magn. Reson. A 110 (1994) 170.

[2] P. Morgan, S. Conolly, G. Scott, A. Macovski, A readout magnet for prepolarized MRI, Magn. Reson. Med. 36 (1996) 527.

[3] H. Zu, S.M. Conolly, G.C. Scott, A. Macovski, Homogeneous magnet design using linear programming, IEEE Trans. Magn. 36 (2000) 476.

[4] R. McDermott, S.-K. Lee, B. ten Haken, A.H. Trabesinger, A. Pines, J. Clarke, Microtesla MRI with a superconducting quantum interference device, PNAS 101 (2004) 7857.

[5] M. Mößle, W.R. Myers, S.-K. Lee, N. Kelso, M. Hatridge, A. Pines, J. Clarke, SQUID-detected in vivo MRI at microtesla magnetic fields, IEEE Trans. Appl. Supercond. 15 (2005) 757.

[6] A.N. Matlachov, P.L. Volegov, M.A. Espy, J.S. George, R.H. Kraus Jr., SQUID detected NMR in microtesla fields, J. Magn. Reson. 170 (2004) 1.

[7] C.H. Tseng, G.P. Wong, V.R. Pomeroy, R.W. Mair, D.P. Hinton, D. Hoffmann, R.E. Stoner, F.W. Hersman, D.G. Cory, R.L. Walsworth, Low-field MRI of laser polarized noble gas, Phys. Rev. Lett. 81 (1998) 3785.

[8] M.P. Augustine, A. Wong-Foy, J.L. Yarger, M. Tomaselli, A. Pines, D.M. TonThat, J. Clarke, Low field magnetic resonance images of polarized noble gases obtained with a dc superconducting quantum interference device, Appl. Phys. Lett. 72 (1998) 1908.

[9] A.K. Venkatesh, A.X. Zhang, J. Mansour, L. Kubatina, C.H. Oh, G. Blasche, M.S. Unlu, D. Balamore, F.A. Jolesz, B.B. Goldberg, M.S. Albert, MRI of the lung gas-space at very low field using hyperpolarized noble gases, Magn. Reson. Imaging 21 (2003) 773.

[10] C.P. Bidinosti, J. Choukeife, P.J. Nacher, G. Tastevin, In vivo NMR of hyperpolarized ^{3}He in the human lung at very low magnetic fields, J. Magn. Reson. 162 (2003) 122.

[11] C.P. Bidinosti, J. Choukeife, G. Tastevin, A. Vignaud, P.J. Nacher, MRI of the lung using hyperpolarized ^{3}He at very low magnetic field (3 mT), Magn. Reson. Mater. Phy. 16 (2004) 255.

[12] H.C. Seton, J.M.S. Hutchison, D.M. Bussel, Gradiometer pick-up coil design for a low field SQUID-MRI system, Magn. Reson. Mater. Phy. 8 (1999) 116.

[13] R.W. Mair, M.I. Hrovat, S. Patz, M.S. Rosen, I.C. Ruset, G.P. Topulos, L.L. Tsai, J.P. Butler, F.W. Hersman, R.L. Walsworth, He-3 lung imaging in an open access, very-low field human magnetic resonance imaging system, Magn. Reson. Med. 53 (2005) 745.

[14] S.-K Lee, M. Mößle, W. Myers, N. Kelso, A.H. Trabesinger, A. Pines, J. Clarke, SQUID-detected MRI at 132 µT with T_1-weighted contrast established at 10 µT–300 µT, Magn. Reson. Med. 53 (2005) 9.

[15] D.G. Norris, J.M.S. Hutchison, Concomitant magnetic field gradients and their effects on imaging at low magnetic field strengths, Magn. Reson. Imaging 8 (1990) 33.

[16] D.A. Yablonskiy, A.L. Sukstanskii, J.J.H. Ackerman, Image artifacts in very low magnetic field MRI: the role of concomitant gradients, J. Magn. Reson. 174 (2005) 279.

[17] T. Classen-Vujcic, J. Slotboom, A.F. Mehlkopf, Reduction of concomitant field gradient effects by main magnetic field alteration, Proc. Soc. Magn. Reson. 3 (1995) 56.

[18] T. Classen-Vujcic, J. Slotboom, A.F. Mehlkopf, Hardware corrections of concomitant field gradients, Proc. Int. Soc. Magn. Reson. Med. 5 (1997) 110.

[19] C.A. Meriles, D. Sakellariou, A.H. Trabesinger, V. Demas, A. Pines, Zero- to low-field MRI with averaging of concomitant gradient fields, PNAS 102 (2005) 1840.

[20] R.M. Weisskoff, M.S. Cohen, R.R. Rzedzian, Nonaxial whole-body instant imaging, Magn. Reson. Med. 29 (1993) 796.

[21] X.J. Zhou, Y.P. Du, M.A. Bernstein, H.G. Reynolds, J.K. Maier, J.A. Polzin, Concomitant magnetic-field-induced artifacts in axial echo planar imaging, Magn. Reson. Med. 39 (1998) 596.

[22] K.F. King, A. Ganin, X.J. Zhou, M.A. Bernstein, Concomitant gradient field effects in spiral scans, Magn. Reson. Med. 41 (1999) 103.

[23] Y.P. Du, X.J. Zhou, M.A. Bernstein, Correction of concomitant magnetic field-induced image artifacts in nonaxial echo-planar imaging, Magn. Reson. Med. 48 (2002) 509.

[24] P.L. Volegov, J.C. Mosher, M.A. Espy, R.H. Kraus Jr., On concomitant gradients in low-field MRI, J. Magn. Reson. 175 (2005) 103.

[25] M.A. Bernstein, X.J. Zhou, J.A. Polzin, K.F. King, A. Ganin, N.J. Pelc, G.H. Glover, Concomitant gradient terms in phase contrast MR: analysis and correction, Magn. Reson. Med. 39 (1998) 300.

[26] P. Volegov, A.N. Matlachov, M.A. Espy, J.S. George, R.H. Kraus Jr., Simultaneous magnetoencephalography and SQUID detected nuclear MR in microtesla fields, Magn. Reson. Med. 52 (2004) 467.

[27] H.W. Fischer, P.A. Rinck, Y. van Haverbeke, R.N. Muller, Nuclear relaxation of human brain gray and white matter: analysis of field dependence and implications for MRI, Magn. Reson. Med. 16 (1990) 317.

[28] R. McDermott, N. Kelso, S.-K. Lee, M. Mößle, M. Mück, W. Myers, B. ten Haken, H.C. Seton, A.H. Trabesinger, A. Pines, J. Clarke, SQUID-detected magnetic resonance imaging in microtesla magnetic fields, J. Low Temp. Phys. 135 (2004) 793.

[29] P.B. Roemer, W.A. Edelstein, C.E. Hayes, S.P. Souza, O.M. Mueller, The NMR phased array, Magn. Reson. Med. 16 (1990) 192.

[30] E.M. Haacke, R.W. Brown, M.R. Thompson, R. Venkatesan, in: Magnetic Resonance Imaging: Physical Principles and Sequence Design, Wiley-Liss, New York, 1999, p. 296.